Journal of Science: Advanced Materials and Devices 9 (2024) 100649

Contents lists available at ScienceDirect

Journal of Science: Advanced Materials and Devices

journal homepage: www.elsevier.com/locate/jsamd

Chirality-dependent energy induced by spin-orbit torque-driven artificial spin texture

Suhyeok An [a], Hyeong-Joo Seo [a,1], Eunchong Baek [a], Ki-Seung Lee [b], Soobeom Lee [c], Jun-Su Kim [a], Chun-Yeol You [a,*]

[a] Department of Physics and Chemistry, DGIST, Daegu, 42988, South Korea
[b] Emerging Materials Science Research Center, DGIST, Daegu, 42988, South Korea
[c] Center for Basic Science, DGIST, Daegu, 42988, South Korea

ARTICLE INFO

Keywords:
Chirality
Noncollinear spin system
Interfacial dzyloshinskii-moriya interaction
Spin-orbit torque

ABSTRACT

Recently, vast research has been under investigation on the role of chirality in magnetization dynamics, an area that currently lacks a comprehensive understanding. To gain further insight into the importance of chirality, we explore the effects of varying the degree of chirality. To investigate these effects, we have fabricated samples with perpendicular magnetic anisotropy symmetry breaking through local helium ion irradiation with various azimuthal angles and degrees of irradiation. In this system, the spin-orbit torque can induce artificial spin texture, and our azimuthal angle and degree of chirality dependent results reveal a clear cosine dependence and a nonlinear increase, respectively. It implies the system not only follows the energy contribution of interfacial Dzyaloshinskii-Moriya interaction but also has a nonlinear impact depending on anisotropy asymmetry induced chirality differences. These experimental observations are consistent with our theoretical model and micromagnetic simulations, supporting our experimental results. Overall, our findings provide further insights into the role of chirality in magnetization dynamics and may have important implications for the development of future magnetic devices.

1. Introduction

Chirality is one of the most important phenomena in diverse fields of science, including physics, chemistry, biology, and materials science. Recently, the exotic role of chirality in magnetic phenomena has been actively investigated. Magnetically induced optical activity was measured in a chiral medium [1]. The observation of a direct relation between spin and chirality using organized organic films of chiral molecules opens the field of chirality induced spin selectivity [2]. In magnetic crystals, nonzero asymmetric exchange coupling induced chirality has been considered theoretically [3,4], and experimental observations have shown that asymmetric exchange coupling induced chiral magnetic order plays a crucial role in the helical spin order [5] and inversion symmetry breaking system [6].

The interfacial Dzyaloshinskii-Moriya interaction (DMI), as an asymmetric exchange coupling with interfacial origins, can also arise in the inversion symmetry breaking systems such as heavy metal (HM)/ferromagnetic metal (FM) bilayers [7]. Here, DMI is unavoidable and performs a great influence on the whole inversion symmetry breaking system, causing various chiral induced static and dynamic phenomena [8]. For these reasons, recently, there are efforts that utilize the chirality in various spintronics fields [9]. One of them, DMI, have been reported as influencing the magnetization switching in an inversion symmetry breaking system, and it results in chirality-induced magnetization switching variation by a magnetic field [10–12], spin-orbit torque (SOT) [13,14], and both [15]. It supposes a clear intervention of chirality on dynamics of magnetization switching, but there are not many clues.

For a deeper understanding, one possible approach is to vary a degree of chirality, which is until not be proceeded. In this work, we directly observe the chirality-dependent system energy based on Hall signal analysis. The system is prepared to possess a lateral symmetry breaking of perpendicular magnetic anisotropy (PMA) by utilizing a local helium ion irradiation (HII). The helium ion irradiated region has a smaller PMA, so we have two different PMA regions. The SOT can induce

Peer review under responsibility of Vietnam National University, Hanoi.
* Corresponding author.
E-mail address: cyyou@dgist.ac.kr (C.-Y. You).
[1] Present address: Department of Materials Science and Engineering, KAIST, Daejeon 34141, South Korea.

https://doi.org/10.1016/j.jsamd.2023.100649
Received 31 July 2023; Received in revised form 6 November 2023; Accepted 16 November 2023
Available online 20 November 2023

artificial chiral spin texture in this structure because of the two different PMA regions. Induced spin texture interacts with the DMI of the system, and it shows a clear nonlinear tendency according to the degree of chirality. Experimental results are also well explained by our theoretical model and micromagnetic simulations, which offer an obvious nonlinear intervention of chirality on magnetization dynamics.

2. Experimental

2.1. Thin film deposition and device fabrication conditions

We used a magnetron sputter for thin film deposition. A DC power source was used for Ta, Pt, and Co deposition, and an AC power source was used for MgO deposition. The resultant stacks were as follows: sample 1: Ta(1.5)/Pt(4)/Co(0.6)/MgO(2)/Ta(2), and sample 2: Ta(3)/Pt(5)/Co(0.8)/MgO(2)/Ta(2). Here, the bottom and top Ta layers are buffer and capping layers, respectively. After the deposition was completed, patterning was performed using a photolithography method, and dry etching was performed through Ar ion milling. Consequently, sample 1 had the following geometry: 5 μm width × 25 μm length in the current line; 5 μm width × 25 μm length in the voltage line. Sample 2 had the following geometry: 10 μm width × 40 μm length in the current line; 3 μm width × 16 μm length in the voltage line.

2.2. Helium ion irradiation process

HII can be used as a method to change the magnetic properties. HII causes structural deformation and interfacial disturbance induced by penetration of high-energy helium ions, and it can modulate the magnetic properties in a local range from microns to tens of nanometers. We adjusted the local PMA of magnetic thin films by using HII. In sample 1, HII was performed in various shapes, and detailed information is shown in Fig. S1. The acceleration voltage of the helium ions was set as 30 kV, and the beam current was 2.1 ± 0.3 pA. Here, the dose was set as 25 ions/nm^2 only. Since the dose is defined as the number of irradiated ions per unit area, the irradiated region was fixed at 200 μm^2 to reduce the error possibly induced by irradiation time differences due to an area change. In sample 2, the acceleration voltage and beam current were 30 kV and 2.5 ± 0.5 pA, respectively. Here, several doses of 15, 30, and 45 ions/nm^2 were irradiated in separate samples. The irradiation area was set to 8 μm width × 40 μm length, where ions only pass through half the area of the sample of 5 μm width × 40 μm length to avoid misalignment-induced errors. The helium ion microscope (Carl Zeiss/ORION Nano-Fab) we used for HII is in the Institute of Next-Generation Semiconductor Convergence Technology in DGIST, South Korea.

2.3. Transport measurement for measuring spin-orbit torque-induced phenomena

To analyze the transport-based SOT phenomena, we used a DC and AC source (Keithley, 6221) and a nanovoltmeter (Keithley, 2182A). The degree of shift in hysteresis loop can be measured with a 2-axis electromagnet system. Before AHE hysteresis loop measurement, a sufficient time should pass (at least 30 s) to obtain a constant in-plane directional external field aligned with current. Then, the loop was measured by swapping z-directional external field while injecting a current, which can result in a sufficient SOT phenomenon. The waiting time between each point of magnetic field was set as 300 ms, and the measurement interval was −1.5 Oe (1.5 Oe) from 500 Oe (−500 Oe) to −500 Oe (500 Oe). Here, to minimize the effect of Joule heating, a pulse current was used, not a DC current. We observed Hall resistance (R_H) while the 100 μs width pulse was injected using a pulse-delta tool supported by 6221-2182A communication.

3. Results and discussion

3.1. Sample preparation

We fabricated two types of thin film samples using DC and AC magnetron sputtering: sample 1: Ta(1.5)/Pt(4)/Co(0.6)/MgO(2)/Ta(2) and sample 2: Ta(3)/Pt(5)/Co(0.8)/MgO(2)/Ta(2). Here, the unit for the number in parentheses is nm. The prepared samples were patterned in the Hall bar geometry using photolithography and argon ion etching. As a next step, for fabricating a precise lateral symmetry breaking system, we utilize the HII technique, which are suitable to modulate local materials properties because of its small beam spot size and long penetration length [16]. Actually, HII can reportedly change magnetic properties such as the anisotropic properties of a magnetic thin film [17–19], exchange bias [20–22], ferromagnetic exchange coupling [23], DMI energy density [24,25], domain wall (DW) motion [26,27], SOT characteristics [28–31], pinning site control [32], and manipulation of skyrmions [33,34]. Among them, we focused on the change in anisotropic characteristic and expected the formation of the spatially asymmetric distribution of magnetizations, which is necessary ingredient for chiral system, through a local anisotropy variation.

First, the magnetic anisotropic property was measured. Because the anisotropic property is sensitive to the degree of HII, we determined the change in the anisotropic property with dose. Here, sample 1 was irradiated with a fixed dose of 25 ions/nm^2, and sample 2 was irradiated with a dose that varied from 0 to 45 ions/nm^2 with a step of 15 ions/nm^2. The magnetic anisotropy was determined using the generalized Sucksmith-Thompson method (see Fig. S2 for more details). The extracted effective anisotropy field (H_K) has a decreasing tendency with dose, and this is a well-known phenomenon [17–19,29,30]. The resultant $\mu_0 H_K$ is as follows: 0.79 and 0.43 T at 0 and 25 ions/nm^2 for sample 1; 1.44, 1.07, 0.95, and 0.76 T at 0, 15, 30, and 45 ions/nm^2 for sample 2, respectively. Note that H_K is the 1st-order effective anisotropy field containing the demagnetization effect. We confirmed that the 2nd-order anisotropy fields are small and negligible in our study. In here, we should mention that all raw data for the R_H loop is measured by a mixture of contribution between pristine H_K and H_K for the selected dose. However, we were able to remove the mixed pristine contribution through appropriate methods, and the resulting data exclusively represents the H_K contribution induced by the selected dose only. In second, the interfacial DMI energy density was also measured for the sample1 and sample 2 at the pristine case (0 ions/nm^2). And the values are −0.71 and −1.45 mJ/m^2 for samples 1 and 2, respectively. Here, the Pt/Co structure has a negative sign of the interfacial DMI energy density and stabilizes the counterclockwise (CCW) Néel-type spin configuration [35,36]. In addition, because the DMI energy density has been reported to be insensitive to HII compared to H_K in a proper range of doses [24,25,33], we assumed that the interfacial DMI energy density is constant for our dose range during analysis. However, the effect caused by a change in the DMI remains, so a careful approach should be used for more complex systems. See Fig. S3 (sample 1) and Fig. S4 (sample 2) for detailed results for extracting the DMI energy density in each sample.

3.2. Theoretical derivations of system energy

To understand the geometry of our system, definitions of $\hat{n}$ and $\hat{\sigma}$ are required. Because the HII is conducted on only part of the samples, the system is divided into irradiated (I-) and nonirradiated (NI-) regions, as shown in Fig. 1. Therefore, the system contains a boundary area between the I- and NI-regions. Here, $\hat{n}$ is defined as the normal vector of the boundary plane from the NI-region to the I-region. $\hat{\sigma}$ is defined as the direction of the spin polarization of the spin current induced by the spin Hall effect (SHE) of the HM layer. Therefore, $\hat{\sigma}$ is set in the $-y$ direction for an electric current flowing in the $+x$ direction because our sample contains a Pt layer whose spin Hall angle (SHA) is known to be positive

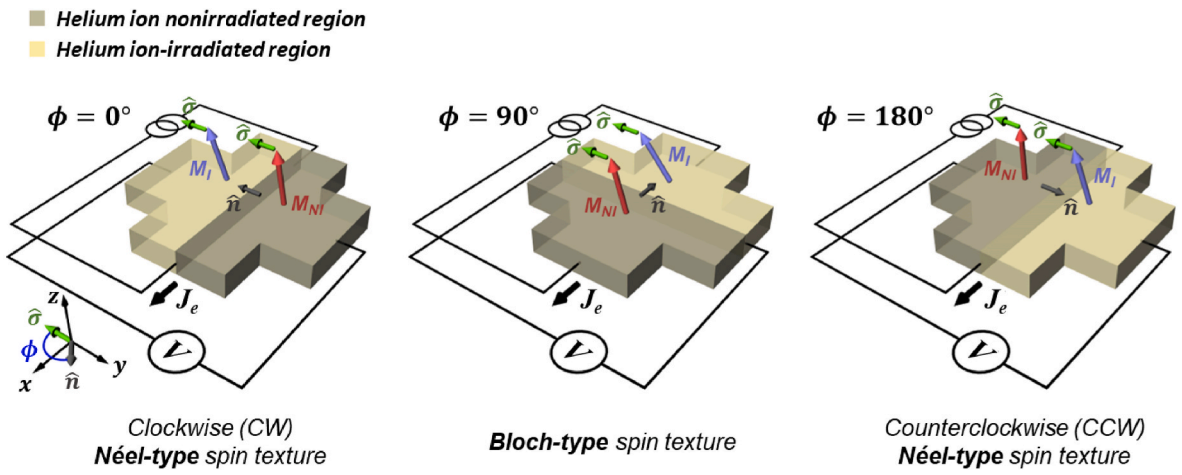

Fig. 1. Schematic diagrams of irradiation position-dependent spin textures. The irradiated (I-) region and nonirradiated (NI-) region are shown in bright and dark yellow, respectively. M_{NI} (M_I) indicates the magnetization in the NI-region (I-region). $\hat{n}$ is a normal vector of the boundary plane directed from the NI-region to I-region. $\hat{\sigma}$ is the direction of the spin polarization from the SHE of the HM layer. φ is determined as the relative azimuthal angle between $\hat{n}$ and $\hat{\sigma}$. Depending on φ, the Néel-type spin texture with CW or CCW chirality appears at $\varphi = 0$ and 180°, while the Bloch-type spin texture appears at $\varphi = 90°$. At the boundary between each region, a chiral spin texture is formed, resulting in system energy variation.

[37]. Therefore, when an electric current is injected into the system, the spin current induced by the SHE affects the FM layer according to $\vec{J_s} = \theta_{SH} \bullet (\hat{\sigma} \times \vec{J_e})$, and the magnetization exerts the damping-like torque (DLT) $\vec{\tau} \sim \hat{m} \times (\hat{\sigma} \times \hat{m})$ induced by SOT. Here, θ_{SH} and $\hat{m}$ are the SHA of the system and unit vector of the magnetization, respectively. Because our system consists of two different H_K regions, the magnetization in each region reacts differently to SOT. This results in different polar angles for the I- and NI-regions: more (less) tilted for the I- (NI-) region. Therefore, an artificially designed inhomogeneous spin configuration is formed at the boundary. Here, the tilted polar angles of M_{NI} (magnetization in the NI-region) and M_I (magnetization in the I-region) are defined as θ_{NI} and θ_I, respectively.

With the presence of a nonzero DMI, the additional energy term between neighboring spins induced by the DMI is expressed as follows.

$$\mathcal{H} = -\sum_{i,j} \vec{D}_{ij} \bullet \left(\vec{m}_i \times \vec{m}_j \right) \tag{1}$$

Here, $\vec{m}_{i(j)}$ is the vector of the $i(j)$-th magnetization, and D_{ij} is the DMI energy constant between $\vec{m}_i$ and $\vec{m}_j$. Through combination with the colinear exchange coupling, the DMI favors specific chiral spin configurations depending on the sign of D_{ij}. Note that the contribution of the DMI in the homogeneous colinear spin configuration region (inside a monodomain) is quenched. However, the inhomogeneous spin configuration region plays an important role similar to the DWs and edges of samples. In our experiments, the role of the DMI becomes important at the boundary between the NI- and I-regions because of the inhomogeneous spin configuration artificially adjusted by SOT. We can calculate the DMI induced system energy through integration of the whole system by considering the inhomogeneous spin region. If the interfacial DMI energy density is almost constant throughout the system, then the system energy can be represented with an inhomogeneous contribution as follows.

$$E^{DMI} = -D_{int} \int_{x_1}^{x_2} \int_{y_1}^{y_2} \sin\theta(x,y) dxdy \tag{2}$$

Here, (x_1, x_2) and (y_1, y_2) are the x- and y-directional boundary conditions of the inhomogeneous area. D_{int} is the interfacial DMI energy density.

Because the SOT influences the magnetizations in the NI- and I-regions differently, an artificial spin texture can be achieved at the boundary of the regions as mentioned above. Here, one can freely decide the position of the I-region. According to the position of the I-region, the spin texture changes from Néel-type to Bloch-type according to the relative angle between $\hat{n}$ and $\hat{\sigma}$, defined as φ, as shown in Fig. 1. Since the DMI of the system favors a specific chirality sign, it produces an energy difference depending on the sign, type and magnitude of the spin texture. In here, we should mention that inhomogeneous spin region contains variety angle range of spins between θ_{NI} and θ_I. But we hypothesis the simplest model and it is considering only two spins of boundary ignoring the complexly distributed remnant spins in noncollinear region. As a result, the energy difference between the spin textures stabilized and destabilized by the DMI is expressed as follows.

$$\Delta E^{DMI} = E^{DMI}_{CCW} - E^{DMI}_{CW} \propto D_{int} \sin\Delta\theta \cos\varphi \tag{3}$$

Here, E^{DMI}_{CCW} and E^{DMI}_{CW} represent the system energies at the CCW and clockwise (CW) spin textures, respectively. Furthermore, one can understand that $\Delta\theta$ is caused by cross-product of spins of boundary and φ is by dot-product with D_{int} vector. $\Delta\theta$ is the relative polar angle difference and defined as $\Delta\theta = \theta_I - \theta_{NI}$. The sign of $\Delta\theta$ can be determined by the direction of the initial magnetization such that $\Delta\theta > 0$ in the up state initialization case and $\Delta\theta < 0$ in the down state initialization case. This is only a very simple toy model of the system, but it explains the main feature of our experimental results well.

3.3. Azimuthal angle dependent system energy

To analyze the effect caused by the artificial spin texture, we measured the φ-dependent SOT-induced effective field in sample 1. The measurement geometry is shown in Fig. 2(a), and the φ-dependent irradiation area information can be found in Fig. S1. When an electric current is injected into the system, an artificial spin texture is formed because of the SOT. This artificially formed spin texture interacts with the DMI of the system, and the total system energy is changed, as seen in Fig. 2(b). When the direction of the electric current is fixed (in the $+x$ direction in the case of the energy diagram), the spin texture of opposite sign is formed according to the up state ($+z$ direction) or down state ($-z$ direction) magnetization: the CW spin texture in the up state and CCW in the down state when $\varphi = 0°$ and the CCW spin texture in the up state and CW in the down state when $\varphi = 180°$. This implies that different variations in the system energy are induced according to the magnetization state because the system DMI is unchangeable. Therefore, the energy differences between the up and down state magnetization should follow

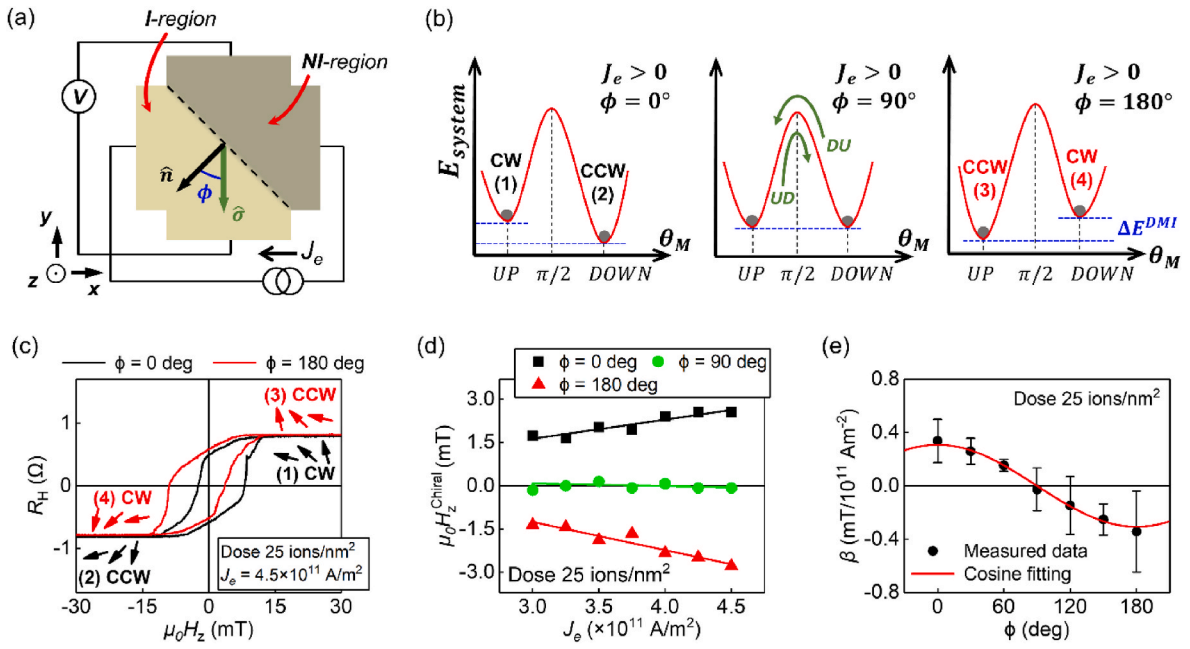

Fig. 2. Observation of H_z^{Chiral} induced by energy differences from artificial spin texture in sample 1. Here, the dose of sample 1 is fixed as 25 ions/nm^2 for various φ. (a) Schematic diagram of the measurement geometry. (b) Diagram of the total system energy at various φ for a fixed current direction. (c) SOT-induced hysteresis loop shift when a current is flowing through the system ($J_e = 4.5 \times 10^{11}$ A/m^2) at $\varphi = 0$ and 180°. Here, each number within parentheses corresponds to the magnetization state in the energy diagram. (d) J_e-dependent H_z^{Chiral} according to φ. The solid lines are linear fittings, and their slope, β, implies the efficiency of H_z^{Chiral} caused by the spin texture. (e) φ-dependent β tendency. The fitting curve is a cosine, shown in red.

Equation (3). And this approach suggests that the energy difference induced by the artificial spin texture can be detected through the magnetization switching process.

To observe the energy difference experimentally, we measured anomalous Hall effect (AHE) hysteresis loops, as shown in Fig. 2(c). For artificial spin texture formation, the injected current density is $J_e = 4.5 \times 10^{11}$ A/m^2 at both $\varphi = 0$ and 180°. As a result, clear shifts of the loop in the positive ($\varphi = 0$) and negative ($\varphi = 180°$) directions are observed, and this shift originates from the chirality reversal accompanying magnetization switching [11,12]. In the case of $\varphi = 0°$, one can understand that UD switching includes chirality reversal from the CW ((1) black arrows) to CCW ((2) black arrows) spin texture, whereas CCW (2) to CW (1) reversal appears in DU switching. Here, because our system possesses intrinsic chirality determined by the DMI, different system energies are derived according to the type of spin texture. In the case of our system, a negative sign of the DMI energy density is induced by the Pt/Co interface, and the CCW spin texture is stabilized. As a result, different energies are required when the chirality reversal follows CW to CCW or CCW to CW, inducing differences in the quantity of the coercive field between UD and DU magnetization switching. Thus, more (less) magnetic field is required for switching the magnetization from the CCW (CW) to CW (CCW) spin texture, which results in a shift of the hysteresis loop. However, at $\varphi = 180°$, the opposite situation occurs. The UD switching includes CCW ((3) red arrows) to CW ((4) red arrows) chirality reversal, whereas DU switching includes CW (4) to CCW (3) chirality reversal. Thus, a different directional shift appears compared with $\varphi = 0°$. This analysis implies that the shift of the hysteresis loop is a result of the energy difference between the spin textures stabilized and destabilized by the DMI of the system. We define H_z^{Chiral} ($\equiv (H_c^{UD} + H_c^{DU})/2$) as the degree of shift of the loop, which acts as an additional magnetic field. Here, H_c^{UD} and H_c^{DU} are the coercive fields in UD and DU switching, respectively. H_z^{Chiral} should be proportional to the chirality induced energy difference as follows:

$$H_z^{Chiral} \propto \Delta E^{DMI} \propto \sin\Delta\theta \cos\varphi \tag{4}$$

According to Equation (4), the shift of the loop is a fingerprint of the formation of the chiral spin texture and chirality-dependent system energy variation.

For a deeper understanding, we introduce an ansatz to describe the degree of the loop shift as an additional effective field, $H_z^{Chiral} = \beta \bullet J_e$ [38]. β is defined as the efficiency of the additional effective field caused by the chiral spin texture. We extracted the current amplitude-dependent H_z^{Chiral} at $\varphi = 0$, 90, 180°, as shown in Fig. 2(d). The results show two different tendencies according to φ. First, when $\varphi = 0/180°$ ($\cos\varphi = \pm 1$), a linear relation of H_z^{Chiral} with the magnitude of the injected electric current is detected. Here, different signs of the slope appear between $\varphi = 0$ and 180°. This is because the sign of the spin texture becomes opposite with the different φ, as mentioned above. The linearity can be understood from Equation (4). If $\Delta\theta$ is small enough, then $\sin\Delta\theta \approx \Delta\theta$. Thus, H_z^{Chiral} can be represented using the PMA energy relation (see Supplementary Information Note 2) as follows.

$$H_z^{Chiral} \propto \Delta\theta \propto h_{y,SOT}\left(\frac{1}{H_K^I} - \frac{1}{H_K^{NI}}\right) \tag{5}$$

Here, $h_{y,SOT}$ is the damping-like torque induced effective field by SOT defined as $h_{y,SOT} = \hbar J_s / 2eM_s t_F$ [39], and $\hbar$, e, M_s, t_F is Planck constant, charge of electron, saturation magnetization, and thickness of ferromagnet layer, respectively. H_K^{NI}, and H_K^I are the effective anisotropy field in the NI-region, and the effective anisotropy field in the I-region, respectively. Because material parameters including the anisotropic properties are constant after fabrication, one can understand that H_z^{Chiral} only depends on $h_{y,SOT}$, as in Equation (5). $h_{y,SOT}$ has a linear relation with the electric current density because the injected spin current is determined by the relation $\vec{J_s} = \theta_{SH} \bullet (\hat{\sigma} \times \vec{J_e})$. Thus, H_z^{chiral} also follows the same linear tendency with the electric current as $H_z^{Chiral} \propto J_e$. Second, at $\varphi = 90°$ ($\cos\varphi = 0$), there is no noticeable change depending on the current density within the error range. This is because the type of spin texture is different at $\varphi = 90°$ compared with $\varphi = 0/180°$. The Néel-type is formed at $\varphi = 0/180°$, while the Bloch-type is formed at $\varphi = 90°$.

Because the Bloch-type spin texture has no chirality-dependent energy difference induced by DMI of system, H_z^{chiral} disappears in the $\varphi = 90°$ case.

3.4. Degree of chirality dependent system energy

From the ansatz, β can be extracted by linear fitting of H_z^{Chiral} versus J_e for each φ. The resultant β versus φ is well fitted by a cosine function, as seen in Fig. 2(e). Based on the cosine behavior of β, the artificial spin texture is rotated from the CW Néel-type ($\varphi = 0°$) to Bloch-type ($\varphi = 90°$) and CCW Néel-type ($\varphi = 180°$) according to the position of the I-region when a positive current is injected into the system. Therefore, it can be understood that the Néel-type spin texture only contribute to the variation of system energy. With this result, the artificial spin texture is confirmed to not only be controllable by SOT but also to influence the system energy.

The Néel-type spin texture induced system energy variations can be detected through the H_z^{Chiral} induced by the system energy variation. Here, one possible expectation is that the degree of spatial asymmetry of the spin texture should depend on the effective anisotropy field difference ($\Delta H_K \equiv H_K^{NI} - H_K^{I}$) because it determines the degree of $\Delta\theta$. Therefore, we proceeded to measure H_z^{Chiral} according to ΔH_K. From the previous φ-dependent β measurement, H_z^{Chiral} is confirmed to be maximized in the case of the Néel-type spin texture. Therefore, we prepared sample 2 by fixing $\varphi = 0°$. The prepared sample 2 results in ΔH_K values of 0, 0.37, 0.49, and 0.68 T at doses of 0, 15, 30, and 45 ions/nm^2, respectively (see the inset of Fig. S2(c) for more details). For a more precise quantification of H_z^{Chiral}, we carried out a measurement process with a 2-axis magnetic field, as shown in Fig. 3(a). The φ-dependent results in section 2.3 only confirmed the formation of a spin texture and its influence on the system energy. However, when the SOT is sufficiently large, a DLT contribution appears simultaneously [38], which causes a greater effect compared to H_z^{Chiral}. Therefore, to precisely analyze the effect of the Néel-type chiral spin texture, the SOT-induced effective field was measured when several x-direction external magnetic fields (H_x) were applied. Therefore, we need to adopt the DLT effective field, $H_z^{DL} = \chi \bullet J_e$, which is determined by the interplay between the DW profile, the DMI of the system and H_x [40,41]. Here, χ corresponds to the efficiency of the DLT induced by SOT.

For each direction of J_e and H_x, H_z^{DL} and H_z^{Chiral} have different tendencies. H_z^{DL} and H_z^{Chiral} have the same sign when H_x is directed in the $+x$ direction regardless of the J_e direction (① and ② diagrams in Fig. 3(a)), and the opposite signs appear for the -x direction of H_x (③ and ④ diagrams in Fig. 3(a)). However, the measured shift of the AHE hysteresis loop gives mixed signals from H_z^{DL} and H_z^{Chiral}.

$$H_z^{eff} \equiv \left(H_C^{UD} + H_C^{DU}\right)/2 = H_z^{DL} + H_z^{Chiral} \tag{6}$$

From the H_x dependence of H_z^{eff}, there should be a difference in the degree of shift of the hysteresis loop depending on the signs of H_z^{DL} and H_z^{Chiral}. As a result, different H_z^{eff} values can be seen in the solid line and dashed line hysteresis loops, as shown in Fig. 3(b). Compared to the solid line, the dashed line hysteresis loop clearly shows a small H_z^{eff}, which corresponds to the case when the signs of H_z^{DL} and H_z^{Chiral} are opposite. For more details, H_z^{eff} is extracted for each current density, and a clear difference is observed depending on the direction of H_x, as shown in Fig. 3(c). Because H_z^{DL} depends on the direction of H_x while having no influence on H_z^{Chiral}, H_z^{Chiral} and H_z^{DL} can be extracted using Equation (6).

$$H_z^{Chiral} = \left[H_z^{eff}(+H_x) + H_z^{eff}(-H_x)\right] / 2 \tag{7}$$

$$H_z^{DL} = \left[H_z^{eff}(+H_x) - H_z^{eff}(-H_x)\right] / 2 \tag{8}$$

The extracted H_z^{Chiral} at 45 ions/nm^2 calculated through Equation (7) is shown in Fig. 3(d). Here, each value of H_z^{Chiral} is average data measured under various H_x, and the error bar is estimated by calculating the standard error.

As a result, H_z^{Chiral} has a larger slope compared to the pristine sample (0 ions/nm^2) as well as a linear tendency with J_e, as seen in Fig. 3(d). From this, we can explain two situations. The first concerns the linearity and odd-functionality of H_z^{Chiral} versus J_e. The SOT behaves as a trigger of spin texture formation, and the direction of the SOT is determined by the direction of the injected electric current. Thus, the odd-functionality can be considered to be the opposite current direction leading to a reversed sign of H_z^{Chiral}. From this, it is verified that the degree of variation of system energy can be artificially adjustable by controlling the current. Second, a larger slope of H_z^{Chiral} occurs compared with the pristine sample (0 ions/nm^2). This means that ΔH_K influences the magnitude of the system energy variation, as we expected. For more perspective, β is extracted by linear fitting of H_z^{Chiral} versus J_e at each ΔH_K. Here, because $h_{y,SOT}$ is proportional to the electric current, Equation (5) can be modified based on the definition of β as follows.

$$\beta = \frac{H_z^{Chiral}}{J_e} \propto \frac{1}{H_K^{I}} - \frac{1}{H_K^{NI}} = \frac{\Delta H_K / H_K^{NI}}{1 - \Delta H_K / H_K^{NI}} \tag{9}$$

We can observe that β tends to increase and well follow the trend from Equation (9), as seen in Fig. 3(e). One of the possible reasons for the increasing trend is the possibility of the formation of a steeper spin texture in a larger ΔH_K system. Although a similar SOT effect is applied to the system (see Fig. S5 for confirming the dose-dependent H_z^{DL} in various dose), a greater asymmetry of the spin texture can be formed in the larger ΔH_K case. This results in a higher energy difference between the spin textures stabilized and destabilized by the DMI.

3.5. Micromagnetic simulation

A micromagnetic simulation was performed to verify the additional effective field induced by chirality reversal using MuMax^3 [42]. For the simulation, the grid size was set as 1 nm × 50 nm × 1 nm in the (x, y, z) dimensions, and the cell size was 1 nm. The material parameters were as follows: $M_S = 1.0$ MA/m; $A_{ex} = 20$ pJ/m; $\alpha = 0.01$; $D_{int} = 1.0$ mJ/m^2. Here, A_{ex}, and α are exchange stiffness and Gilbert damping constant, respectively. The noncollinear spin texture is formed through the y-axis direction, which is achieved by setting different uniaxial anisotropy energies (K_U). The larger K_U of the system is fixed at 0.6 MJ/m^3, and the smaller K_U is varied from 0.5975 to 0.58 MJ/m^3. To implement the PMA state, the easy axis is set to the z-axis.

When a $h_{y,SOT}$ is applied by the SOT, each magnetization in larger and smaller K_U reacts differently according to its PMA energy. If the direction of $h_{y,SOT}$ is not changed, then one can also understand that the chirality differs between the up and down states. Therefore, when the external magnetic field in the z-direction is switched, chirality reversal also simultaneously occurs. As a result, a shift of the hysteresis loop also occurs in the opposite direction, as seen in Fig. 4(a).

From our toy model, the degree of shift in the hysteresis loop is proportional to $D_{int}\Delta\theta$ in the proper range of D_{int} and $\Delta\theta$. Here, D_{int} is the interfacial DMI energy density, and $\Delta\theta$ is the angle difference at the boundary of the chiral region. In the result, we can observe that not only is H_z^{chiral} linearly related to $h_{y,SOT}$ but also its sign becomes opposite at opposite D_{int}, as seen in Fig. 4(b). This tendency implies that the chirality reversal-induced hysteresis loop shift is governed by the DMI of the system. Because the interfacial DMI stabilizes the Néel-type spin texture, an energy difference induced by chirality reversal occurs only when the spin texture is Néel-type. Therefore, when we rotate the $h_{y,SOT}$ in the xy plane, H_z^{chiral} should follow a cosine behavior because the Bloch-type contribution occurs when the in-plane bias becomes off-axis relative to y. This can be seen in Fig. 4(c).

One of the parameters that affects the energy difference during chirality reversal is the PMA energy difference (ΔK_U) of the two regions.

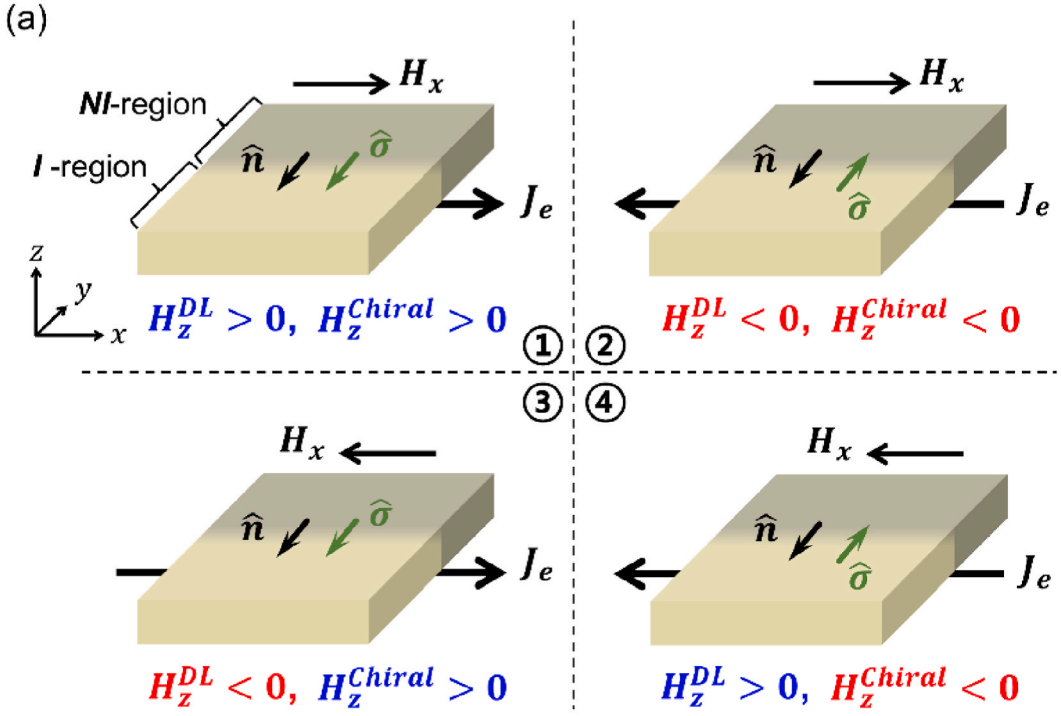

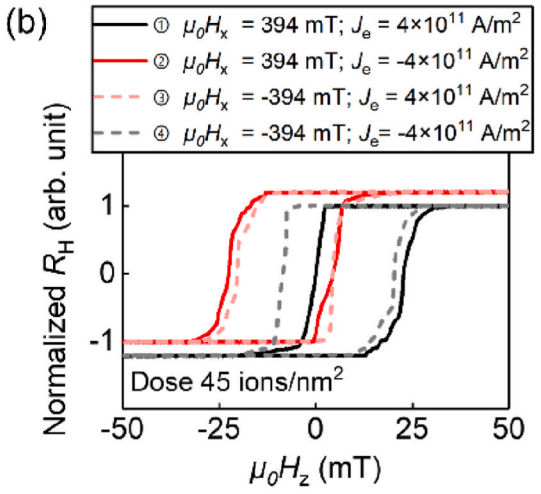

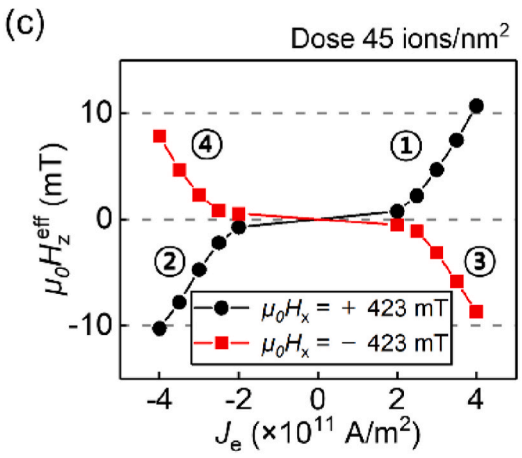

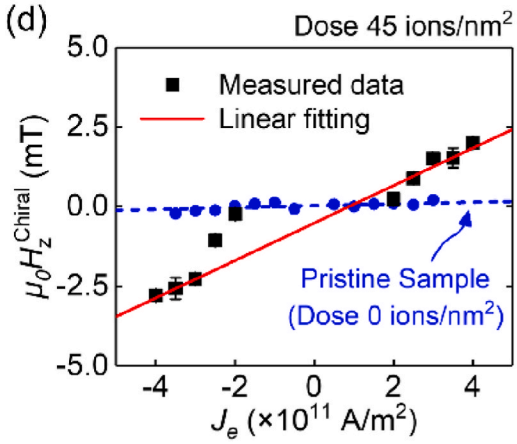

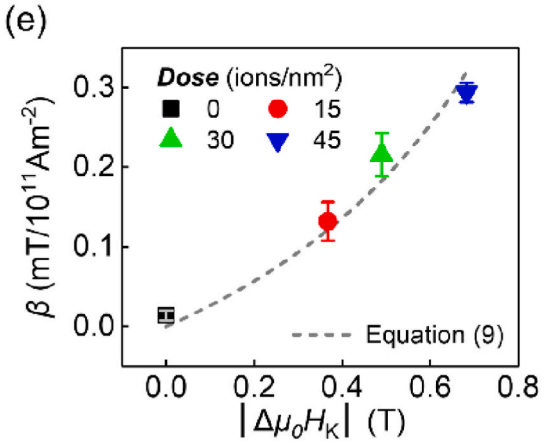

(caption on next page)

Fig. 3. System energy variation according to the asymmetry of the spin texture in sample 2. (a) Schematic diagram of four cases according to the directions of H_x and J_e. The signs of H_z^{DL} and H_z^{Chiral} are the same in the ① and ② diagrams and opposite in the ③ and ④ diagrams, depending on the direction of H_x. (b) Shift of the hysteresis loop at $|\mu_0 H_x| = 394$ mT, $|J_e| = 4.0 \times 10^{11}$ A/m^2, and a dose of 45 ions/nm^2. The solid curve is at positive H_x, and the dashed curve is for the negative case. (c) Measured H_z^{eff} and (d) extracted H_z^{Chiral} according to J_e at 45 ions/nm^2. The red line is the linear fitting, and the error bar is from the average value of H_z^{Chiral} at various H_x. The blue points and blue dashed line indicate the extracted H_z^{Chiral} and linear fitting for the pristine sample (0 ions/nm^2). (e) ΔH_K-dependent slope, β, extracted for each dose. ΔH_K can be estimated by calculating the H_K differences between the nonirradiated region and irradiated region. Here, the gray dashed line indicates the trend curve calculated by Eq. (9).

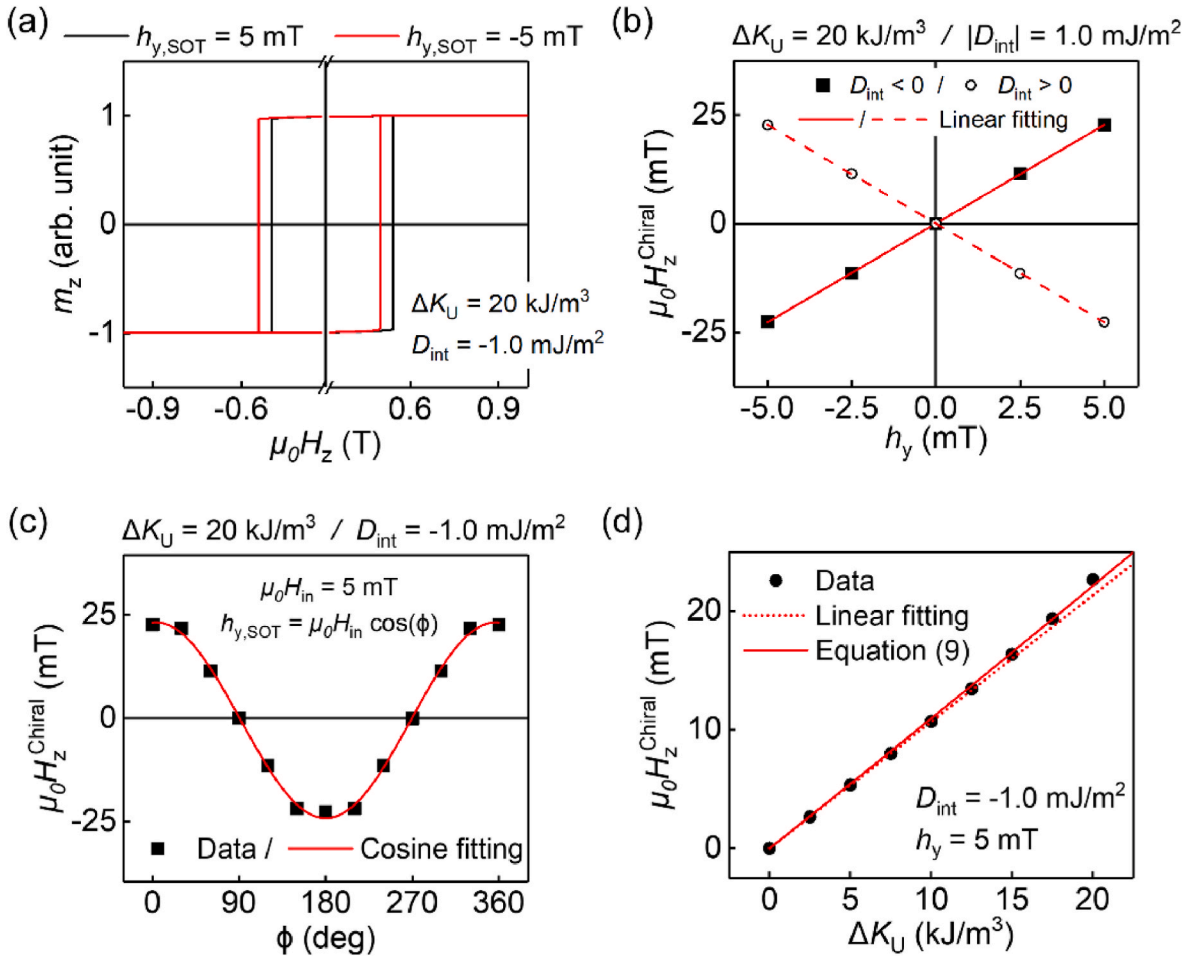

Fig. 4. Chirality reversal-induced additional effective field (H_z^{chiral}) simulation. (a) Hysteresis loop simulation according to the direction of $h_{y,SOT}$. (b) Degree of H_z^{chiral} at various magnitudes of $h_{y,SOT}$ for positive and negative interfacial DMI energy densities. (c) Bias field azimuthal angle-dependent and (d) PMA energy difference-dependent H_z^{chiral}. Here, dotted line is linear fitting considering $\Delta K_U \leq 5kJm^{-3}$ and solid curve is fitting result by equation (9).

Because different ΔK_U values result in different boundary conditions of the spin texture in the chiral region, variations in H_z^{chiral} also occur. The relation between ΔK_U and the hysteresis loop shift has already been reported to have a similar tendency with ΔK_U [15,38]. However, according to Fig. 4(d), the tendency is slightly off from linear at higher ΔK_U. The nonlinearity can be described more precisely by Equation (9), which suggests that our toy model explains the behavior of system energy by the SOT-induced artificial spin texture quite exactly in proper ranges of material parameters.

4. Conclusion

In summary, the system energy variation by chiral spin texture induced by SOT is directly observed in φ and ΔH_K dependences. We confirm the clear cosine dependence in φ and nonlinear increasement in ΔH_K variations. It is also predicted in our theoretical models and the micromagnetic simulation shows similar tendencies with experimental results. These variations suggests an obvious intervention of chirality on the system energy variation, and our finding offers more perspective on chiral system and its utilization on spin systems.

Declaration of competing interest

The authors declare that they have no known competing financial interests or personal relationships that could have appeared to influence the work reported in this paper.

Acknowledgements

This work is supported by the National Research Foundation of Korea (NRF-2020M3F3A2A02082437, NRF-2021M3F3A2A01037522, NRF-2021R1A2C2007672, NRF-2018R1A6A3A11041061).

Appendix A. Supplementary data

Supplementary data to this article can be found online at https://doi.org/10.1016/j.jsamd.2023.100649.

References

[1] G.L.J.A. Rikken, E. Raupach, Observation of magneto-chiral dichroism, Nature 390 (1997) 493–494, https://doi.org/10.1038/37323.

[2] K. Ray, S.P. Ananthavel, D.H. Waldeck, R. Naaman, Asymmetric scattering of polarized electrons by organized organic films of chiral molecules, Science 283 (1999) 814–816, https://doi.org/10.1126/science.283.5403.814.

[3] I. Dzyaloshinsky, A thermodynamic theory of "weak" ferromagnetism of antiferromagnetics, J. Phys. Chem. Solid. 4 (1958) 241–255, https://doi.org/10.1016/0022-3697(58)90076-3.

[4] T. Moriya, Anisotropic superexchange interaction and weak ferromagnetism, Phys. Rev. 120 (1960) 91–98, https://doi.org/10.1103/PhysRev.120.91.

[5] M. Uchida, Y. Onose, Y. Matsui, Y. Tokura, Real-space observation of helical spin order, Science 311 (2006) 359–361, https://doi.org/10.1126/science.1120639.

[6] M. Bode, M. Heide, K. von Bergmann, P. Ferriani, S. Heinze, G. Bihlmayer, A. Kubetzka, O. Pietzsch, S. Blügel, R. Wiesendanger, Chiral magnetic order at surfaces driven by inversion asymmetry, Nature 447 (2007) 190–193, https://doi.org/10.1038/nature05802.

[7] A.R. Fert, Magnetic and transport properties of metallic multilayers, Mater. Sci. Forum 59–60 (1991) 439–480. https://doi.org/10.4028/www.scientific.net/MSF.59-60.439.

[8] M. Shen, X. Li, Y. Zhang, X. Yang, S. Chen, Effects of interfacial Dzyaloshinskii–Moriya interaction on magnetic dynamics, J. Phys. D Appl. Phys. 55 (2022), 213002, https://doi.org/10.1088/1361-6463/ac4366.

[9] S.-H. Yang, R. Naaman, Y. Paltiel, S.S.P. Parkin, Chiral spintronics, Nat. Rev. Phys. 3 (2021) 328–343, https://doi.org/10.1038/s42254-021-00302-9.

[10] D.-S. Han, N.-H. Kim, J.-S. Kim, Y. Yin, J.-W. Koo, J. Cho, S. Lee, M. Kläui, H.J. M. Swagten, B. Koopmans, C.-Y. You, Asymmetric hysteresis for probing dzyaloshinskii–moriya interaction, Nano Lett. 16 (2016) 4438–4446, https://doi.org/10.1021/acs.nanolett.6b01593.

[11] D.-S. Han, K. Lee, J.-P. Hanke, Y. Mokrousov, K.-W. Kim, W. Yoo, Y.L.W. van Hees, T.-W. Kim, R. Lavrijsen, C.-Y. You, H.J.M. Swagten, M.-H. Jung, M. Kläui, Long-range chiral exchange interaction in synthetic antiferromagnets, Nat. Mater. 18 (2019) 703–708, https://doi.org/10.1038/s41563-019-0370-z.

[12] Z. Luo, T.P. Dao, A. Hrabec, J. Vijayakumar, A. Kleibert, M. Baumgartner, E. Kirk, J. Cui, T. Savchenko, G. Krishnaswamy, L.J. Heyderman, P. Gambardella, Chirally coupled nanomagnets, Science 363 (2019) 1435–1439, https://doi.org/10.1126/science.aau7913.

[13] N. Perez, E. Martinez, L. Torres, S.-H. Woo, S. Emori, G.S.D. Beach, Chiral magnetization textures stabilized by the Dzyaloshinskii-Moriya interaction during spin-orbit torque switching, Appl. Phys. Lett. 104 (2014), 092403, https://doi.org/10.1063/1.4867199.

[14] S. An, H.-J. Seo, E. Baek, S. Lee, C.-Y. You, Role of the chiral spin configuration in field-free spin–orbit torque-induced magnetization switching by a locally injected spin current, Appl. Phys. Lett. 120 (2022), 262402, https://doi.org/10.1063/5.0094631.

[15] H. Wu, J. Nance, S.A. Razavi, D. Lujan, B. Dai, Y. Liu, H. He, B. Cui, D. Wu, K. Wong, K. Sobotkiewich, X. Li, G.P. Carman, K.L. Wang, Chiral symmetry breaking for deterministic switching of perpendicular magnetization by spin–orbit torque, Nano Lett. 21 (2021) 515–521, https://doi.org/10.1021/acs.nanolett.0c03972.

[16] G. Hlawacek, V. Veligura, R. van Gastel, B. Poelsema, Helium ion microscopy, J. Vac. Sci. Technol. B 32 (2014), 020801, https://doi.org/10.1116/1.4863676.

[17] C. Chappert, H. Bernas, J. Ferré, V. Kottler, J.-P. Jamet, Y. Chen, E. Cambril, T. Devolder, F. Rousseaux, V. Mathet, H. Launois, Planar patterned magnetic media obtained by ion irradiation, Science 280 (1998) 1919, https://doi.org/10.1126/science.280.5371.1919. –1922.

[18] T. Devolder, Light ion irradiation of Co/Pt systems: structural origin of the decrease in magnetic anisotropy, Phys. Rev. B 62 (2000) 5794–5802, https://doi.org/10.1103/PhysRevB.62.5794.

[19] T. Devolder, J. Ferré, C. Chappert, H. Bernas, J.-P. Jamet, V. Mathet, Magnetic properties of He + -irradiated Pt/Co/Pt ultrathin films, Phys. Rev. B 64 (2001), 064415, https://doi.org/10.1103/PhysRevB.64.064415.

[20] C. Wang, C. Chen, C.-H. Chang, H.-S. Tsai, P. Pandey, C. Xu, R. Böttger, D. Chen, Y.-J. Zeng, X. Gao, M. Helm, S. Zhou, Defect-induced exchange bias in a single SrRuO 3 layer, ACS Appl. Mater. Interfaces 10 (2018) 27472–27476, https://doi.org/10.1021/acsami.8b07918.

[21] P. Kuświk, A. Gaul, M. Urbaniak, M. Schmidt, J. Aleksiejew, A. Ehresmann, F. Stobiecki, Tailoring perpendicular exchange bias coupling in Au/Co/NiO systems by ion bombardment, Nanomaterials 8 (2018) 813, https://doi.org/10.3390/nano8100813.

[22] C.J. Jensen, A. Quintana, M. Sall, L.H. Diez, J. Zhang, X. Zhang, D. Ravelosona, K. Liu, Ion irradiation and implantation modifications of magneto-ionically induced exchange bias in Gd/NiCoO, J. Magn. Magn Mater. 540 (2021), 168479, https://doi.org/10.1016/j.jmmm.2021.168479.

[23] L. Koch, F. Samad, M. Lenz, O. Hellwig, Manipulating the energy balance of perpendicular-anisotropy synthetic antiferromagnets by He + -ion irradiation, Phys. Rev. Appl. 13 (2020), 024029, https://doi.org/10.1103/PhysRevApplied.13.024029.

[24] H.T. Nembach, E. Jué, K. Poetzger, J. Fassbender, T.J. Silva, J.M. Shaw, Tuning of the Dzyaloshinskii–Moriya interaction by He + ion irradiation, J. Appl. Phys. 131 (2022), 143901, https://doi.org/10.1063/5.0080523.

[25] A. Sud, S. Tacchi, D. Sagkovits, C. Barton, M. Sall, L.H. Diez, E. Stylianidis, N. Smith, L. Wright, S. Zhang, X. Zhang, D. Ravelosona, G. Carlotti, H. Kurebayashi, O. Kazakova, M. Cubukcu, Tailoring interfacial effect in multilayers with Dzyaloshinskii–Moriya interaction by helium ion irradiation, Sci. Rep. 11 (2021), 23626, https://doi.org/10.1038/s41598-021-02902-y.

[26] L.H. Diez, M. Voto, A. Casiraghi, M. Belmeguenai, Y. Roussigné, G. Durin, A. Lamperti, R. Mantovan, V. Sluka, V. Jeudy, Y.T. Liu, A. Stashkevich, S.M. Chérif, J. Langer, B. Ocker, L. Lopez-Diaz, D. Ravelosona, Enhancement of the Dzyaloshinskii-Moriya interaction and domain wall velocity through interface intermixing in Ta/CoFeB/MgO, Phys. Rev. B 99 (2019), 054431, https://doi.org/10.1103/PhysRevB.99.054431.

[27] X. Zhao, B. Zhang, N. Vernier, X. Zhang, M. Sall, T. Xing, L.H. Diez, C. Hepburn, L. Wang, G. Durin, A. Casiraghi, M. Belmeguenai, Y. Roussigné, A. Stashkevich, S. M. Chérif, J. Langer, B. Ocker, S. Jaiswal, G. Jakob, M. Kläui, W. Zhao, D. Ravelosona, Enhancing domain wall velocity through interface intermixing in W-CoFeB-MgO films with perpendicular anisotropy, Appl. Phys. Lett. 115 (2019), 122404, https://doi.org/10.1063/1.5121357.

[28] X. Zhao, Y. Liu, D. Zhu, M. Sall, X. Zhang, H. Ma, J. Langer, B. Ocker, S. Jaiswal, G. Jakob, M. Kläui, W. Zhao, D. Ravelosona, Spin–orbit torque driven multi-level switching in He + irradiated W–CoFeB–MgO Hall bars with perpendicular anisotropy, Appl. Phys. Lett. 116 (2020), 242401, https://doi.org/10.1063/5.0010679.

[29] P. Dunne, C. Fowley, G. Hlawacek, J. Kurian, G. Atcheson, S. Colis, N. Teichert, B. Kundys, M. Venkatesan, J. Lindner, A.M. Deac, T.M. Hermans, J.M.D. Coey, B. Doudin, Helium ion microscopy for reduced spin orbit torque switching currents, Nano Lett. 20 (2020) 7036–7042, https://doi.org/10.1021/acs.nanolett.0c02060.

[30] S. An, E. Baek, J.-A. Kim, K.-S. Lee, C.-Y. You, Improved spin–orbit torque induced magnetization switching efficiency by helium ion irradiation, Sci. Rep. 12 (2022) 3465, https://doi.org/10.1038/s41598-022-06960-8.

[31] T. Lee, J. Kim, S. An, S. Jeong, D. Lee, D. Jeong, N.J. Lee, K.-S. Lee, C.-Y. You, B.-G. Park, K.-J. Kim, S. Kim, S. Lee, Field-free spin-orbit torque switching of GdCo ferrimagnet with broken lateral symmetry by He ion irradiation, Acta Mater. 246 (2023), 118705, https://doi.org/10.1016/j.actamat.2023.118705.

[32] J.H. Franken, M. Hoeijmakers, R. Lavrijsen, J.T. Kohlhepp, H.J.M. Swagten, B. Koopmans, E. van Veldhoven, D.J. Maas, Precise control of domain wall injection and pinning using helium and gallium focused ion beams, J. Appl. Phys. 109 (2011), 07D504, https://doi.org/10.1063/1.3549589.

[33] R. Juge, K. Bairagi, K.G. Rana, J. Vogel, M. Sall, D. Mailly, V.T. Pham, Q. Zhang, N. Sisodia, M. Foerster, L. Aballe, M. Belmeguenai, Y. Roussigné, S. Auffret, L. D. Buda-Prejbeanu, G. Gaudin, D. Ravelosona, O. Boulle, Helium ions put magnetic skyrmions on the track, Nano Lett. 21 (2021) 2989–2996, https://doi.org/10.1021/acs.nanolett.1c00136.

[34] L.-M. Kern, B. Pfau, V. Deinhart, M. Schneider, C. Klose, K. Gerlinger, S. Wittrock, D. Engel, I. Will, C.M. Günther, R. Liefferink, J.H. Mentink, S. Wintz, M. Weigand, M.-J. Huang, R. Battistelli, D. Metternich, F. Büttner, K. Höflich, S. Eisebitt, Deterministic generation and guided motion of magnetic skyrmions by focused He + -ion irradiation, Nano Lett. 22 (2022) 4028–4035, https://doi.org/10.1021/acs.nanolett.2c00670.

[35] H. Yang, A. Thiaville, S. Rohart, A. Fert, M. Chshiev, Anatomy of dzyaloshinskii-moriya interaction at Co/Pt interfaces, Phys. Rev. Lett. 115 (2015), 267210, https://doi.org/10.1103/PhysRevLett.115.267210.

[36] Y.-K. Park, D.-Y. Kim, J.-S. Kim, Y.-S. Nam, M.-H. Park, H.-C. Choi, B.-C. Min, S.-B. Choe, Experimental observation of the correlation between the interfacial Dzyaloshinskii–Moriya interaction and work function in metallic magnetic trilayers, NPG Asia Mater. 10 (2018) 995–1001, https://doi.org/10.1038/s41427-018-0090-x.

[37] L. Liu, O.J. Lee, T.J. Gudmundsen, D.C. Ralph, R.A. Buhrman, Current-induced switching of perpendicularly magnetized magnetic layers using spin torque from the spin Hall effect, Phys. Rev. Lett. 109 (2012), 096602, https://doi.org/10.1103/PhysRevLett.109.096602.

[38] G. Yu, P. Upadhyaya, Y. Fan, J.G. Alzate, W. Jiang, K.L. Wong, S. Takei, S. A. Bender, L.-T. Chang, Y. Jiang, M. Lang, J. Tang, Y. Wang, Y. Tserkovnyak, P. K. Amiri, K.L. Wang, Switching of perpendicular magnetization by spin–orbit torques in the absence of external magnetic fields, Nat. Nanotechnol. 9 (2014) 548–554, https://doi.org/10.1038/nnano.2014.94.

[39] A.V. Khvalkovskiy, V. Cros, D. Apalkov, V. Nikitin, M. Krounbi, K.A. Zvezdin, A. Anane, J. Grollier, A. Fert, Matching domain-wall configuration and spin-orbit torques for efficient domain-wall motion, Phys. Rev. B 87 (2013), 020402, https://doi.org/10.1103/PhysRevB.87.020402.

[40] C.-F. Pai, M. Mann, A.J. Tan, G.S.D. Beach, Determination of spin torque efficiencies in heterostructures with perpendicular magnetic anisotropy, Phys. Rev. B 93 (2016), 144409, https://doi.org/10.1103/PhysRevB.93.144409.

[41] T. Dohi, S. Fukami, H. Ohno, Influence of domain wall anisotropy on the current-induced hysteresis loop shift for quantification of the Dzyaloshinskii-Moriya interaction, Phys. Rev. B 103 (2021), 214450, https://doi.org/10.1103/PhysRevB.103.214450.

[42] A. Vansteenkiste, J. Leliaert, M. Dvornik, M. Helsen, F. Garcia-Sanchez, B. Van Waeyenberge, The design and verification of MuMax3, AIP Adv. 4 (2014), 107133, https://doi.org/10.1063/1.4899186.